Advanced Science

ADVANCED SCIENCE Open Access

www.advancedscience.com

RESEARCH ARTICLE OPEN ACCESS

Activating Hidden Magnons With Anomalous Rotational Symmetry

Dirk Wulferding[1] | Francesco Gabriele[2] | Wojciech Brzezicki[3] | Mario Cuoco[2] | Changyoung Kim[4] | Veronica Granata[5] | Mariateresa Lettieri[2] | Anita Guarino[2] | Antonio Vecchione[2] | Rosalba Fittipaldi[2] | Filomena Forte[2]

[1]Department of Physics and Astronomy, Sejong University, Seoul, Republic of Korea | [2]CNR-SPIN, c/o Università di Salerno, Fisciano (SA), Italy | [3]Institute of Theoretical Physics, Jagiellonian University, Kraków, Poland | [4]Department of Physics and Astronomy, Seoul National University, Seoul, Republic of Korea | [5]Department of Industrial, Electronic and Mechanical Engineering of Roma Tre University, Rome, Italy

Correspondence: Filomena Forte (filomena.forte@spin.cnr.it)

Received: 26 May 2026 | **Revised:** 1 October 2026 | **Accepted:** 22 October 2026

Keywords: correlated electron systems | mixed-parity magnons | raman spectroscopy

ABSTRACT

Correlated materials with competing spin–orbit and crystal-field interactions can host composite spin–orbital magnons that are highly susceptible to structural and electronic perturbations, enabling the control of magnetic dynamics beyond spin-only physics. Using Raman spectroscopy on Ca_2RuO_4, we show that the partial substitution of Ru with Mn reconstructs the magnon spectrum and reveals one–magnon modes that are hidden in the undoped state. We demonstrate that the transition-metal substitution activates otherwise symmetry-forbidden magnon modes through mirror-symmetry breaking of the underlying spin–orbital configuration. This effect can be theoretically explained by the local structural distortions induced in the RuO_6 octahedra near the dopant, which enable the observation of mixed-parity one–magnon modes. These excitations display a distinctive polarization dependence, with a lowering from fourfold to twofold rotational symmetry arising from the mixed-parity character of the coupled magnons and interference between resonant and nonresonant scattering channels. Our results show that spin–orbit–lattice entanglement provides a route to tailoring collective magnetic excitations and their polarization response in spin–orbit–coupled correlated systems.

1 | Introduction

Spin–orbit coupling (SOC) in correlated electron systems can fundamentally reshape magnetic ground states and excitations, giving rise to phenomena that go beyond conventional spin-only descriptions. When SOC, crystal-field splittings, and electron correlations are of comparable magnitude, spin, orbital, and lattice degrees of freedom become strongly entangled, enabling unconventional forms of magnetism and collective excitations [1–5]. Understanding how these intertwined interactions respond to controlled perturbations is a central challenge in the study of quantum materials.

Ca_2RuO_4 is a prototypical spin–orbit–coupled Mott insulator that exhibits anomalous ground-state responses and a rich phase diagram [6–12] arising from the interplay of spin, orbital, and lattice degrees of freedom [11, 13–17], with still debated properties, particularly about the metal–insulator transition under nonequilibrium conditions [18–26]. Below the metal–insulator transition temperature, the distortions of the RuO_6 octahedra become more

Dirk Wulferding and Francesco Gabriele contributed equally to this study.

This is an open access article under the terms of the Creative Commons Attribution License, which permits use, distribution and reproduction in any medium, provided the original work is properly cited.
© 2026 The Author(s). *Advanced Science* published by Wiley-VCH GmbH

pronounced, and an antiferromagnetic insulating phase emerges with a Néel temperature $T_N \approx 110$ K [9, 27–29]. While initially described in terms of localized $S = 1$ moments of Ru^{4+} ($4d^4$), it is now understood that the magnetism of Ca_2RuO_4 arises from a competition between SOC and crystal-field effects, leading to a spin–orbital–entangled ground state [14, 16, 30–33]. Ca_2RuO_4 is thus close in proximity to a d^4 excitonic magnet, in which long-range order emerges from the coupling of spin–orbit excitons rather than from preformed local moments [34–37]. Magnetic excitations in Ca_2RuO_4 reflect this entanglement, exhibiting strong anisotropy, sizable excitation gaps, and modes with mixed spin–orbital character, as revealed by neutron scattering, Raman and resonant inelastic scattering spectroscopies [14, 16]. A challenging feature of this material is the sensitivity of its magnetic properties to lattice distortions. Changes induced by temperature, pressure, strain, or chemical substitution can reconstruct the magnetic ground state [31, 38–46]. This pronounced spin–orbital–lattice coupling makes Ca_2RuO_4 an ideal platform for exploring how symmetry breaking and structural perturbations can be exploited to tune collective magnetic dynamics in spin–orbit–coupled correlated materials.

The observability of collective magnetic excitations is governed by crystal symmetry and experimental selection rules. As a consequence, a portion of the magnon spectrum may remain hidden, being symmetry–forbidden. Optical and neutron–scattering studies have revealed that structural perturbations, reduced dimensionality, or hybridization with lattice degrees of freedom can render otherwise forbidden one–magnon modes observable [47, 48]. Hybrid magnon–phonon excitations [49] and nonreciprocal magnons [50] further illustrate how subtle symmetry breaking [51–53] can dramatically reshape magnetic excitation spectra. To probe these spectral changes, polarization–resolved Raman spectroscopy serves as a powerful tool, as the polarization of light encodes the symmetry of collective excitations [54–57]. Particularly under resonant conditions, additional scattering pathways can substantially reshape the Raman response and its symmetry signatures, providing direct insight into modifications of both the magnetic and light–matter interactions.

Despite these insights, controlled pathways to activate hidden magnons in bulk spin–orbit correlated materials, without inducing a global structural phase transition, remain scarce. Addressing this gap is crucial to establishing spin–orbital–lattice engineering as a viable route for controlling collective magnetic excitations in correlated materials. In this manuscript, we exploit the design path of transition–metal substitution in Ca_2RuO_4 and demonstrate that it can reconfigure the spin–orbital magnon spectrum, leading to the emergence of one–magnon modes hidden in the pristine material. Our Raman results, supported by theoretical modeling, reveal that these hidden one–magnon excitations are activated by the breaking of mirror symmetry within the spin–orbital manifold. This effect, driven by local RuO_6 octahedral distortions near the dopants, induces the mixing of even- and odd-parity states, thereby enabling the realization of mixed-parity magnon modes. We further uncover an unconventional polarization dependence of the magnon modes emerging upon transition–metal substitution, characterized by a reduction from fourfold to twofold rotational symmetry. We attribute this lowered symmetry to the mixed-parity character of the coupled magnons and to interference between resonant and nonresonant scattering channels.

2 | Evidence of Hidden Magnons and Rotational Symmetry Breaking

To investigate the impact of Mn substitution on the magnetic excitations of Ca_2RuO_4, we perform Raman spectroscopic measurements at cryogenic temperatures. Raman spectroscopy is a useful technique for directly probing magnetic excitations in ruthenates in the form of one- and multi-magnon modes [30, 58, 59], whose energies are directly related to the magnetic correlations between Ru ions. Ca_2RuO_4 belongs to the orthorhombic space group Pbca (#61). For Raman measurements within the crystallographic ab plane, this space group yields excitations of A_g and of B_{1g} symmetry. In Figure 1a, we plot temperature dependent Raman data taken on $Ca_2(Ru,Mn)O_4$ with 0%, 3%, 5%, and 10% Mn content. The outcomes at 0% are completely consistent with those reported in the literature [30]. We can identify T_N for each compound through various Raman fingerprints: at the onset of long-range magnetic order, an A_g phonon around 15 meV experiences significant spin-phonon coupling, leading to discontinuous behavior in energy, linewidth, and intensity [60] (see Figure S3 and Table S2). In addition, an enhanced, featureless background exists at high temperatures ($T > T_N$) due to scattering on incoherent magnetic correlations. Below T_N, this signal disappears for energies smaller than the two-magnon gap [61] (this is most clearly seen in Figure 1a for the sample with 0% Mn below ~ 60 meV, and in Figure S4). We note that similar enhanced scattering backgrounds have been observed in related low-dimensional spin systems in Raman spectroscopy above the ordering temperature [58, 62, 63]. Simultaneously, new one–magnon peaks, marked by arrows in each panel, emerge below T_N. For a better comparison of the evolution of phononic and magnetic excitations with increasing Mn content, we plot individual spectra of all four compounds obtained at a base temperature of $T = 4$ K in Figure 1b. One–magnon modes are shaded, while partially overlapping phonons are marked by asterisks. The pure Ca_2RuO_4 sample hosts a sharp and intense single one–magnon excitation at 12.5 meV (yellow-shaded), which is consistent with the previous report [30]. A partial substitution of Ru with 3% and 5% Mn yields two one–magnon branches with reduced intensity and increased linewidth (shaded green and red), while for a larger Mn content of 10% only a single, broadened and asymmetric magnon mode (yellow-shaded) can be resolved. The extracted parameters and energies are summarized in Table S1, and one– magnon energy and intensity as a function of Mn content are plotted in Figure 1c,d. Consequently, even a small level of substitution shifts the one–magnon mode to higher energies and leads to the emergence of an additional magnetic peak, with a maximum intensity at an energy separation of approximately 1 meV. Further increases in Mn concentration continue to raise the magnon energy and result in a pronounced broadening of the spectral intensity, such that the two split peaks can no longer be distinguished. We further note that Mn–Ru substitution gives rise to additional low–energy magnetic excitations characterized by weak intensity and a broad continuum extending from approximately 5 to 8 meV. The associated spectral weight shows a slight increase with increasing Mn concentration. In addition to the low-energy magnetic modes,

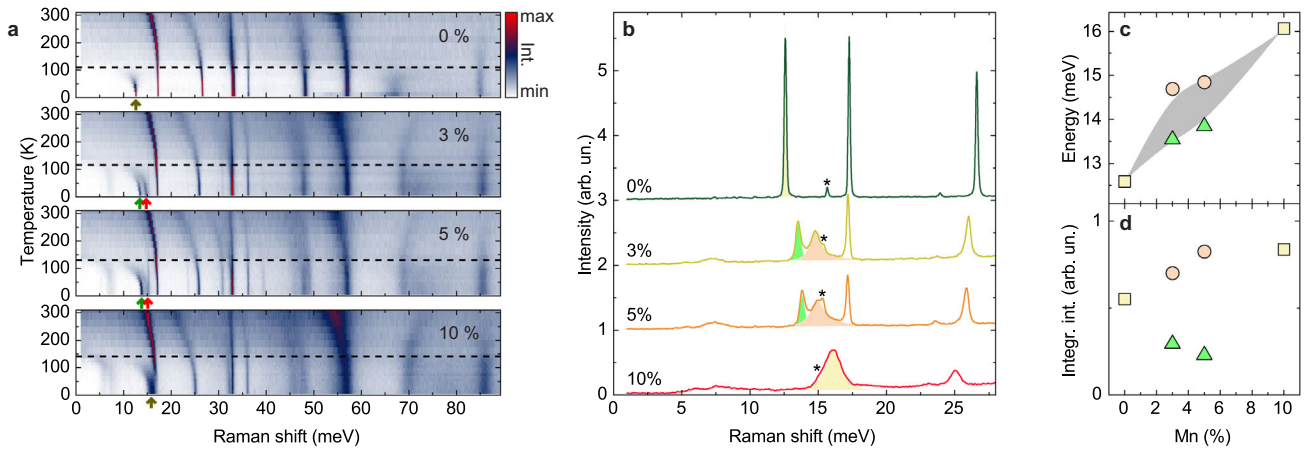

FIGURE 1 | Temperature and doping dependence of magnons in $Ca_2(Ru,Mn)O_4$. (a), Temperature-dependent Raman spectra of $Ca_2(Ru,Mn)O_4$ with 0%, 3%, 5%, and 10% Mn content measured in the B_{1g} symmetry channel. Dashed lines mark the Néel temperatures. The arrows indicate one–magnon excitations. (b), Individual Raman spectra measured at $T = 4$ K. One–magnon contributions are shaded. The black asterisks mark a phonon that partially overlaps with magnons. (c), Magnon energies and (d), their integrated intensities as a function of Mn content.

two extra phononic peaks emerge near the phonon excitations at around 31 and 48 meV as a consequence of Mn substitution, where the former one can be associated with an activated A_g mode. Their detailed evolution is shown in Figure S5. By contrast, no significant modifications are observed in the higher-energy features within the 70–90 meV range.

Here, we concentrate on the one–magnon excitations in the cross-polarization channel, as they exhibit the most pronounced reconstruction upon substituting Ru with Mn.

A deeper insight into the symmetry properties of all observed Raman-active excitations can be gained from polarization-resolved experiments. Figure 2a illustrates three fundamental scattering configurations by relating the polarization vectors of incident and outgoing light to the crystal orientation. In the color contour plot shown in Figure 2b, we detail the evolution of the Raman scattering intensities for individual excitations as a function of light polarization, measured on the 3% Mn sample in crossed polarization (i.e., B_{1g}-selective). Note that all phonon modes (17 meV and higher) show a four-fold periodicity, as expected for modes of B_{1g} symmetry.

In contrast, the two lowest-lying excitations, corresponding to the two branches of one–magnon excitations and marked by green and red arrows, deviate from this behavior and display a two-fold distortion on top of their four-fold periodicity. To emphasize this distortion, and to compare it among the four different samples of our study, we extract the intensity linecuts as shown in the polar plots of Figure 2c–f. Strikingly, in samples where both magnon branches are resolved (i.e., in the 3% and 5% Mn samples), we find a distinct alternating, out-of-phase behavior for the intensity profiles of the two magnons, which may be taken as a consequence of the mixed-parity character of the magnons.

Magnetic excitations of B_{1g} symmetry adhere to a four-fold, d-wave-like intensity profile, where the scattering process is fully described by the Loudon–Fleury (LF) theory [64]. Conversely, in the presence of additional, non-LF terms [57, 65–67], this symmetry may be lowered toward a two-fold distorted pattern. Such non-LF terms may be significantly enhanced through resonance processes. To uncover the presence and relevance of these non-F contributions, we therefore compare the observed one–magnon intensity profiles probed with a $\lambda = 561$ nm laser ($E_{\text{photon}} = 2.21$ eV) to profiles measured with a $\lambda = 660$ nm laser ($E_{\text{photon}} = 1.87$ eV). We quantify the degree of deviation from conventional LF theory by taking the ratio of lobe intensities measured along the 0°-to-180° axis vs. intensities measured along the 90°-to-270° axis. These two configurations are defined as $B_{1g}^{(1)}$ and $B_{1g}^{(2)}$, corresponding to the cases in which the incident light polarization vector is rotated by 90° with respect to the crystal axes (Figure 2a). The resultant ratios are plotted in panels 2g-j for samples with 0%, 3%, 5%, and 10% Mn, respectively, measured at $T = 4$ K. Remarkably, even though the chosen laser energies are not strictly resonant, the intensity ratios in Figure 2g–j demonstrate that the one–magnon mode intensity as a function of light polarization visibly deviates from the symmetrical four-fold pattern characteristic of a pure B_{1g} response (which would correspond to a ratio of 1). This asymmetry clearly indicates that resonant non-LF terms are non-negligible, as detailed in the following section. Moreover, the data reveal that the effect of this proximity to resonance not only evolves systematically as a function of Mn concentration, but also displays distinctly different behaviors depending on the specific one–magnon branch (where resolved).

3 | Modeling Magnon Spectra

In Ca_2RuO_4 the Ru^{4+} ions host four electrons in the t_{2g} shell, giving rise to local orbital and spin moments $L = 1$ and $S = 1$. At the atomic level, the intraionic SOC term $\lambda\,\mathbf{L}\cdot\mathbf{S}$ stabilizes a nonmagnetic $J = 0$ ground state, separated from the excited $J = 1$ and $J = 2$ multiplets. The competition between SOC and electron–lattice interactions — notably the flattening, rotation, and tilting of the RuO_6 octahedra — drives the system away from the ideal $J = 0$ configuration. Consequently, the low-energy manifold forms a quasi-triplet composed of the $J = 0$ singlet and the two lowest components of the $J = 1$ triplet [34]. These

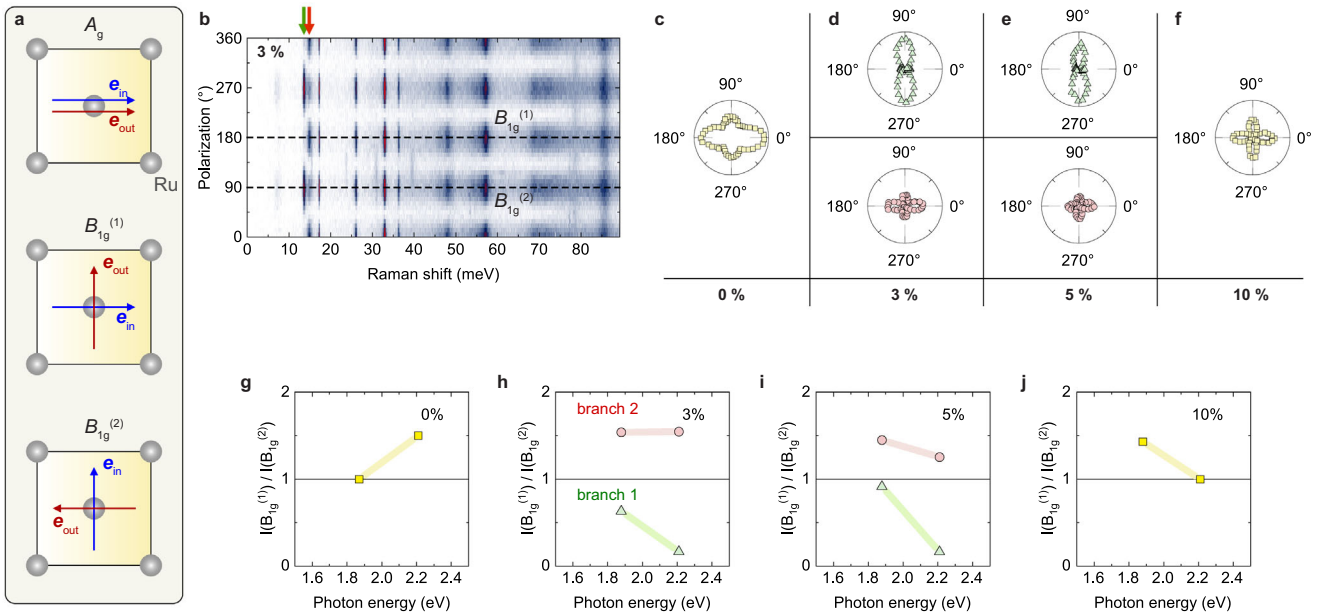

FIGURE 2 | Evolution of the polarization-resolved magnon spectrum in $Ca_2(Ru,Mn)O_4$. (a), Schematic sketch of Raman scattering configurations in different symmetry channels. The polarization vectors of incident and outgoing light (blue and red, respectively) are indicated with respect to the Ru atoms (grey spheres). (b), Polarization-resolved Raman spectra of $Ca_2(Ru,Mn)O_4$ (Mn = 3%) measured at $T = 4$ K with $\epsilon_{in} \perp \epsilon_{out}$. The two individually resolved one–magnon excitations are marked by a green (lower branch) and a red (higher branch) arrow. (c–f), Extracted linecuts of the one–magnon mode intensity as a function of light polarization. In panels **c** and **f** the yellow squares denote the single peaks observed in samples with 0% and 10% Mn content. In panels **d** and **e** the green triangles trace the lower branches, while the red circles mark the higher branches in samples with 3% and 5% Mn content. (g–j), Degree of asymmetry, quantified as the intensity ratio of lobes, as a function of photon energy for all four samples.

states define an effective local moment **T** with total pseudospin $T = 1$, schematically illustrated in Figure 3a in terms of its spin–orbital composition.

Within this pseudospin basis, one can write the nearest-neighbor exchange interactions derived in the strong-coupling limit of the multi-orbital correlated model for the d electrons in the RuO_2 planes (see Note S3). For bonds along the x direction, the effective Hamiltonian reads

$$\mathcal{H}_x = \sum_{\langle i,j\rangle \| x} \left[J_{xx} T_i^x T_j^x + J_{xy} T_i^y T_j^y + J_z T_i^z T_j^z \right], \qquad (1)$$

where J_{xx}, J_{xy}, and J_z are the anisotropic exchange couplings allowed by the orthorhombic symmetry. An analogous form $\mathcal{H}_y$ applies for bonds along y, with $J_{yy} = J_{xx}$ and $J_{yx} = J_{xy}$.

Local symmetry-lowering distortions, including the flattening, rotation and tilting of the RuO_6 octahedra, introduce additional on-site staggered contributions [68]

$$\mathcal{H}_{\text{loc}} = E_T \sum_j (T_j^z)^2 + \delta_c \sum_j (-1)^j (T_j^x T_j^y + T_j^y T_j^x) + \delta_b \sum_j (-1)^j [T_j^z (T_j^x + T_j^y) + (T_j^x + T_j^y) T_j^z], \qquad (2)$$

where E_T is the single-ion anisotropy due to axial compression along the c axis, and δ_c, δ_b represent the anisotropy terms associated with staggered octahedral rotations and tilts about the c and b axes, respectively.

In our model, the effects of impurities at dilute concentrations mainly affect the local crystal field environment. Specifically, since Mn enters with a d^3 non-Jahn Teller configuration, the substitution tends to symmetrize the octahedral Ru–O bonds by reducing the tetragonal energy splitting Δ_T. Hence, we effectively assume that the Mn dopant amplifies the amplitude of the E_T term, as it scales as λ^2/Δ_T [14].

We now describe the symmetry aspects of the low energy magnon modes that are crucial to account for their reconstruction upon Mn substitution. The low-energy spin–orbital states of the t_{2g} manifold ($L = 1, S = 1$) couple anisotropically to the lattice via octahedral compression, rotation about the c axis, and tilting relative to the b axis. These states can be classified by their parity under the vertical mirror operation $\mathcal{M}_b$ (Figure 3a). Specifically, the local ground-state singlet (adiabatically connected to the $J = 0$ state) is $\mathcal{M}_b$-odd, whereas the excited doublet ($J = 1$ subspace) comprises states of opposite parity. In the effective magnetic exchange model, these map to the $T = 1$ states $\{|\tilde{1}\rangle, |\tilde{0}\rangle, |-\tilde{1}\rangle\}$, which diagonalize the local Hamiltonian of Equation (2) and satisfy the aforementioned symmetry constraints, as explicitly shown in the Note S4.

In pristine Ca_2RuO_4, the vertical mirror symmetry is globally preserved within the lattice, and the corresponding mirror-parity quantum number governs the selection rules for magnetic excitations and their coupling to external probes, including Raman scattering. In the full Hamiltonian $\mathcal{H}$, this symmetry is properly defined by the operator $\mathbb{M} \equiv M \otimes \prod_j \mathcal{M}_b^j$, which combines the local action $\mathcal{M}_b^j$ on site j with the spatial mirror

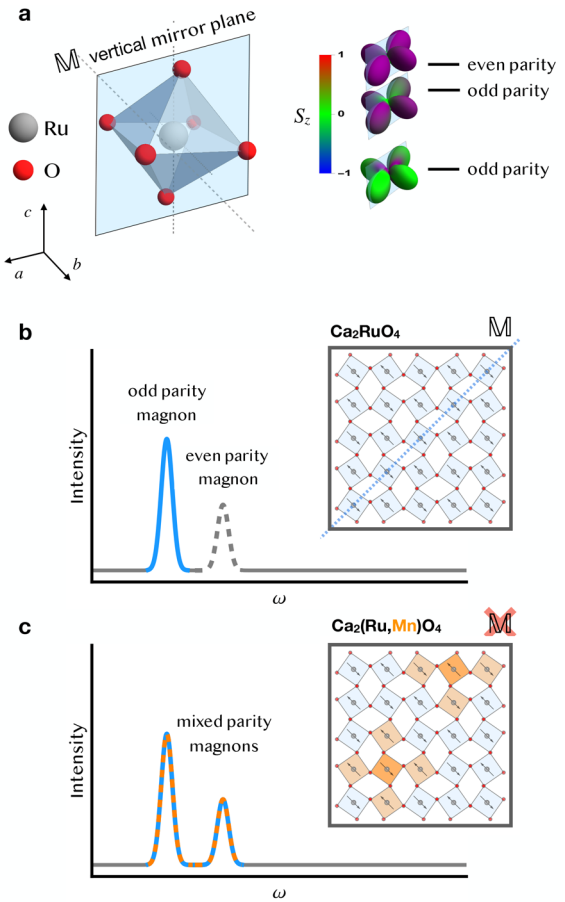

FIGURE 3 | Spin–orbital states and mirror–symmetry breaking in Ca_2RuO_4. (a), Schematic of the three lowest-lying local spin–orbital states stabilized by SOC and octahedral distortions in Ca_2RuO_4. The RuO_6 octahedra tilting relative to the b axis mixes orbital characters, splitting the multiplets into states of definite parity with respect to the diagonal vertical mirror (ac plane perpendicular to the b axis). The lowest-energy state has odd parity, while the higher-energy doublet comprises even and odd parity states. The panel illustrates a representative case associated with a specific sign of the parameter δ_c as related to the staggering of the octahedral rotations about to the c axis; for the opposite sign, the parity of these two states is inverted. (b,c), Schematic of the evolution of the magnon spectrum for the antiferromagnetic state from the undoped (panel **b**) to the Mn-doped configuration (panel **c**), where Mn substitution breaks the diagonal vertical mirror ($\mathbb{M}$). This symmetry breaking activates a one–magnon mode in the cross polarization channel that is silent in the Ca_2RuO_4 compound. Here, we focus on the excitations of the Ru magnetic moments, with the oxygen degrees of freedom projected out. This allows applying a mirror transformation to the Ru lattice and the associated spin configuration, as illustrated in (b).

M mapping the coordinates as $(x, y) \xrightarrow{M} (-y, -x)$. Consequently, two symmetry-distinct one–magnon branches, $|\Psi_-\rangle$ and $|\Psi_+\rangle$, are expected; these branches are odd and even, respectively, under the mirror operation, such that $\mathbb{M}|\Psi_-\rangle = -|\Psi_-\rangle$ and $\mathbb{M}|\Psi_+\rangle = |\Psi_+\rangle$. An explicit demonstration of this symmetry based construction is provided in the Note S4. Assuming the local terms dominate, we perform a perturbative expansion in the exchange coupling and derive the energies of the two magnons relative to the ground-state energy E_0, which at leading order in δ_b and δ_c are expressed as

$$E_- - E_0 = f_0 + \frac{2\delta_b^2}{E_T} + \left(2 - \frac{E_T}{J_{xx} + J_{xy}}\right)\frac{\delta_c^2 \delta_b^2}{E_T^3}, \tag{3}$$

$$E_+ - E_0 = f_0 + \frac{4\delta_b^2}{E_T} + \left(4 + \frac{2E_T}{J_{xx} + J_{xy}}\right)\frac{\delta_c^2 \delta_b^2}{E_T^3}, \tag{4}$$

with $f_0 = E_T - 2\left(J_{xx} + J_{xy}\right) - \delta_c^2 / \left[4\left(J_{xx} + J_{xy}\right)\right]$. These expressions for the one–magnon modes naturally account for the energy shift induced by an increase in the anisotropy magnetic energy E_T, as well as for the emergence of split magnon modes, whose energy separation depends on both the magnitude of the octahedral distortions and the strength of the magnetic exchange.

To describe the Raman spectra, we adopt the LF framework [64]. The Raman scattering operator, whose derivation is detailed in Note S3, is defined as:

$$R \propto \sum_{\langle i,j \rangle} (\boldsymbol{\epsilon}_{\text{in}} \cdot \mathbf{r}_{ij})(\boldsymbol{\epsilon}_{\text{out}} \cdot \mathbf{r}_{ij})\, \mathcal{H}_{ij}, \tag{5}$$

where $\boldsymbol{\epsilon}_{\text{in}}$ and $\boldsymbol{\epsilon}_{\text{out}}$ are the incoming and outgoing polarization vectors, and $\mathcal{H}_{ij}$ denotes the Hamiltonian on bond $\langle i, j \rangle$, which includes both exchange interactions $\mathcal{H}_x$ and $\mathcal{H}_y$ [64].

When the light polarizations are confined to the ab plane, $\boldsymbol{\epsilon}_{\text{in(out)}}$ can be specified by their in-plane angles with respect to a crystallographic axis, such as the a axis. In the B_{1g} geometry adopted in the experiments, the Raman operator reduces to

$$R_{B_{1g}} = \sum_{\langle i,j \rangle_x} \mathcal{H}_{ij} - \sum_{\langle i,j \rangle_y} \mathcal{H}_{ij}, \tag{6}$$

In pure Ca_2RuO_4, only one one–magnon branch is observed in Raman scattering within the B_{1g} symmetry channel (schematically depicted in Figure 3b). As demonstrated in Note S5, the scattering amplitude of the $R_{B_{1g}}$ Raman operator defined in Equation (6) is non-vanishing for this state, since local symmetry breaking mixes the one- and multi-magnon manifolds, allowing the bilinear LF operator to access this excitation.

The selective visibility of a single one–magnon mode is determined by two factors: (i) the symmetry of the Raman tensor, which transforms as odd under the mirror operation $\mathbb{M}$, and (ii) the symmetry of the magnetic exchange Hamiltonian, which, in contrast, is even under $\mathbb{M}$. As a result, only a single one–magnon branch, whose mirror parity is compatible with the Raman tensor (i.e., odd), can couple to light in the B_{1g} channel. The other branch, which is even under $\mathbb{M}$, remains Raman inactive in this symmetry channel and allowed in the A_g symmetry. However, the experimental observations here and in the literature [30] indicate that this magnetic mode is fully obscured in the A_g channel due to the spin–phonon coupling. This is commonly observed in magnetic materials because fully symmetric magnetic excitations hybridize strongly with A_g phonons, leading to pronounced screening and damping of the spectral-weight. The appearance of an additional B_{1g} Raman-active magnon in Mn-substituted samples thus signals a lowering of the local symmetry and the onset of mixed mirror-parity

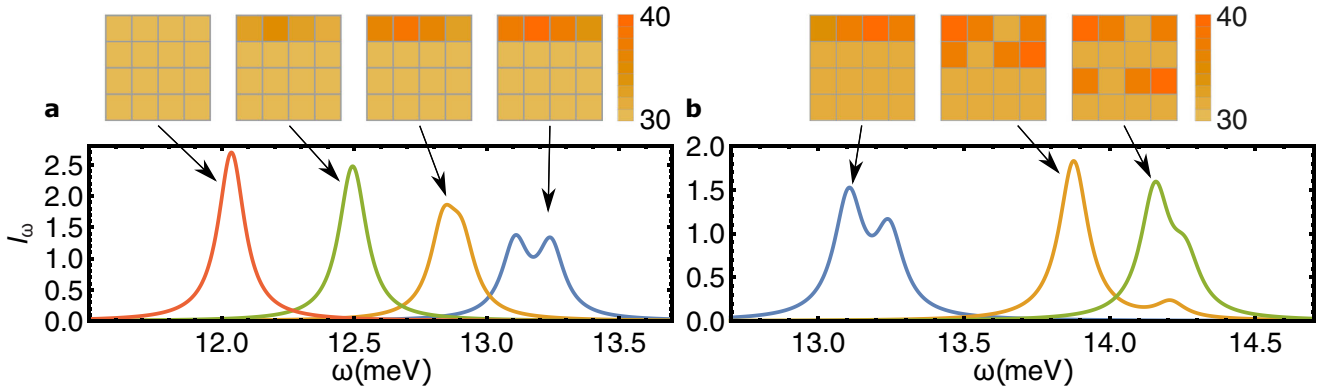

FIGURE 4 | Raman spectral function of a cluster with anisotropic magnetic perturbations. The spectra were evaluated for a 4×4 cluster with periodic boundary conditions and in the presence of inhomogeneous anisotropic magnetic energy E_T nearby the substituted site (corresponding to the darkest orange square in the schematic cluster). (a), Undoped and single-impurity configurations; (b), two-impurity configurations. The parameters of the model are $J_{xx} = 5.2, J_{xy} = 3.1, J_z = 2, E_T = 30$ (in units of meV) at host sites. At the impurity sites the anisotropic magnetic energy E_T is modified to acquire the value $E_T = 40$ and is also varied at the neighboring sites of the impurity, as illustrated by the contour map. For clarity we employ Lorentzian distributions for the spectral function with broadening factor $\eta = 0.06$ meV.

character in the magnetic excitations, as schematically shown in Figure 3c.

In this context, the substitution of Ru by Mn in $Ca_2Ru_{1-x}Mn_xO_4$ drives this effect acting as a local symmetry-breaking perturbation. Previous studies on Mn-doped Ca_2RuO_4 report local structural relaxations around the impurity sites, which in turn lead to concomitant modifications of the magnetic order [41]. However, X-ray measurements on Mn-doped Ca_2RuO_4, including our structural characterization detailing the conservation of the macroscopic *Pbca* space group (see Figure S1) consistent with the data on the same sample batches reported in a previous study [41], confirm the absence of a global structural phase transition. The observation of sharp, coherent Raman peaks throughout the sample indicates that these symmetry-breaking distortions do not originate from highly localized clusters. Rather, the homogeneously distributed dopants create local structural gradients that collectively activate the macroscopic magnonic excitations. This is further corroborated by Energy Dispersive Spectroscopy (EDS) mapping analysis (see Figure S2), which confirms the stoichiometric accuracy and a spatially homogeneous Mn distribution at the sub-micrometric level. We can therefore assume that Mn ions locally relax the octahedral compression around the impurity sites without disrupting the long-range structural order of the crystal.

To substantiate the symmetry-based results discussed previously, we perform exact-diagonalization (ED) calculations of the Raman spectrum on finite clusters, with various distributions of Mn impurities. The calculations are carried out using the full pseudospin Hamiltonian $\mathcal{H} = \mathcal{H}_{loc} + \mathcal{H}_x + \mathcal{H}_y$. The Raman operator $R_{B_{1g}}$ is implemented according to Equation (6), and the Raman intensity spectral function is given by

$$I(\omega) = \sum_n |\langle n|R_{B_{1g}}|\Psi_0\rangle|^2 \, \delta(\omega - E_n + E_0) \, . \tag{7}$$

In Figure 4a,b, we present representative cases for both the undoped and single-impurity configurations, and the two-impurity configurations, respectively. Our focus is on the lowest-energy magnon mode, which is most relevant for the experimental observations. In the undoped case, a single one–magnon mode can be reproduced at approximately 12 meV assuming the following model parameters, $J_{xx} = 5.2$ meV, $J_{xy} = 3.1$ meV, $J_z = 2$ meV, $E_T = 30$ meV which are compatible with the magnetic properties of Ca_2RuO_4 [14, 33].

The introduction of an impurity breaks the vertical mirror symmetry by inducing a short-range anisotropic structural distortion around the impurity, consistent with the orthorhombicity of the crystal lattice. Depending on the magnitude of this local structural change, the strength of the mirror-symmetry breaking can be tuned, resulting in a shift of the emerging double-peak magnon structure to higher energies (Figure 4a). Increasing the number of impurities, e.g., from one to two as in Figure 4b, modulates the relative intensity of the two peaks and redistributes the magnon spectral weight, depending on the positions of the impurities relative to the magnetic sublattice and the gradient profile of the structural potential. When averaging over different impurity configurations, these effects produce a shift in the magnon energies and a finite broadening of the Raman spectral intensity.

The resulting outcomes can reproduce the qualitative changes of the Raman spectra observed in the experiments as a function of the Mn concentration. In particular, the microscopic framework introduced thus far explains why, experimentally, the activated one–magnon mode exhibits a considerable spectral weight compared to that of the pristine peak, as shown in Figure 1b. First, the impurity-induced crystal-field potential and structural gradients affect multiple adjacent Ru spins, ensuring a substantial scattering amplitude for the mixed-parity modes. Furthermore, whereas the pristine mode predominantly retains the character of the symmetry-allowed Ψ_- excitation, the emergent mode originates from the hidden Ψ_+ magnon. As indicated by the approximate expressions given in Equation (4), this makes the corresponding excitation energy highly susceptible to the diverse landscape of local strain and exchange interactions

created by the dopant distribution, leading to a larger energy dispersion.

Finally, we discuss the implications of the angular polarization dependence of the Raman intensity for the mixed-parity magnons. As shown in Figure 2, the one–magnon peaks exhibit a non-trivial angular dependence upon the polarization angle, providing crucial insight into the symmetry properties of the excitations. We first consider the pristine Ca_2RuO_4 system, where the B_{1g} one–magnon mode deviates significantly from the standard four-fold d-wave-like intensity profile predicted by the non-resonant LF theory (see Figure 2c,g). This deviation is particularly pronounced at an incident energy of 2.2 eV, suggesting the breakdown of the non-resonant approximation due to the proximity to a resonance. Far from resonance, the Raman operator $\mathcal{R}$ is governed by the LF theory. As highlighted by Equation (5), this operator is symmetric under the exchange of incident and scattered polarization vectors. Near resonance, however, the perturbative expansion underlying the LF approximation breaks down. In this regime, an antisymmetric contribution to the Raman tensor—arising from intermediate-state transitions that break the exchange symmetry of the incoming and outgoing photon polarizations—emerges and acquires significant spectral weight [65]. We point out that including these resonant terms preserves the validity of our previous analysis: while the standard LF theory robustly explains the emergence of impurity-induced hidden magnons, adding these resonant effects is a necessary refinement to precisely reproduce the polarization-angle dependence of the intensity.

Defining θ as the angle between the incident polarization vector and e.g. the a crystallographic axis, the effective Raman operator in the B_{1g} configuration is modeled as:

$$\mathcal{R} \propto \frac{1}{2}\cos(2\theta)R_{LF} + R_{res}, \tag{8}$$

where the first term represents the symmetric LF contribution, while R_{res} denotes the θ-independent resonant term. This resonant term, R_{res}, arises from transitions to intermediate states within the explicit Raman scattering amplitude [65, 66]. Under resonant conditions, these intermediate transitions activate the antisymmetric components of the Raman tensor. Being rotationally invariant, this antisymmetric term does not modulate with θ. Consequently, under resonant conditions, the total Raman intensity is described by a constant background superimposed on the standard symmetric modulation. This profile is shown in Figure 5a, which displays the calculated intensity obtained by setting the matrix elements of the operator in Equation (8) to values that reproduce the experimental intensity ratio between the two polarization configurations rotated by 90°, for the specific case at 2.2 eV (see Figure 2c,g).

In the Mn-doped system, the scenario is fundamentally modified by the local breakdown of the lattice mirror symmetry, $\mathbb{M}$, induced by impurities. Experimentally, we observe two distinct one–magnon peaks with approximately two-fold symmetries that are mutually phase-shifted by 90° (see Figures 2d,e,h,i). This phenomenology indicates two concurrent effects driven

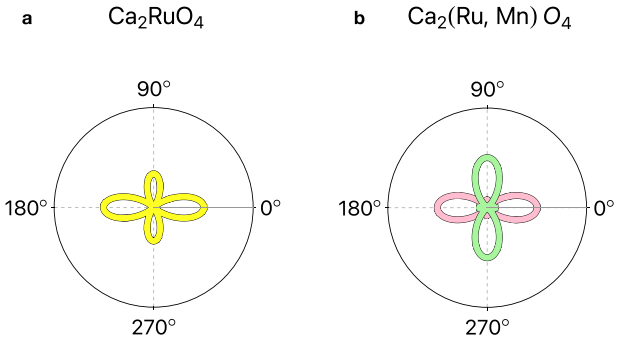

FIGURE 5 | Calculated angular Raman intensity profiles highlighting symmetry breaking in Mn-doped Ca_2RuO_4. (a), Pristine Ca_2RuO_4 system: The intensity profile (yellow line) follows the superposition of a symmetric B_{1g} term ($\cos 2\theta$) and an isotropic resonant background, resulting in an anisotropic 4-fold symmetry. The calculated profile assumes a representative ratio of 1.5 between the 90° phase-shifted intensities, corresponding approximately to the maximum lobe intensity ratio shown in Figure 2g. Further details on the specific values of the matrix elements derived from Equations (9) and (10) can be found in the Note S6. (b), Mn-doped system: The symmetry breaking leads to two distinct modes, $|n_1\rangle$ (green) and $|n_2\rangle$ (pink). The interplay between parity mixing and resonant scattering results in two-fold symmetric lobes that are phase-shifted by 90°. The angular profile was calculated using a mixing angle $\alpha = \pi/8$ and matrix elements optimized to reproduce the $x = 5\%$ (2.2 eV) intensity ratios from Figure 2i. Further details are provided in the Note S6.

by symmetry breaking: the hybridization between one–magnon states and resonance effects.

First, we note that the dopant-induced mirror symmetry breaking hybridizes the original modes into mixed-parity states. Specifically, the two resulting one–magnon eigenstates, denoted as $|n_1\rangle$ and $|n_2\rangle$, arise from the parity mixing of the odd (allowed) $|\Psi_-\rangle$ state and the even (hidden) $|\Psi_+\rangle$ state, defined by a mixing angle α:

$$\begin{pmatrix} |n_1\rangle \\ |n_2\rangle \end{pmatrix} = \begin{pmatrix} \cos\alpha & \sin\alpha \\ -\sin\alpha & \cos\alpha \end{pmatrix} \begin{pmatrix} |\Psi_-\rangle \\ |\Psi_+\rangle \end{pmatrix}. \tag{9}$$

The mirror-plane breaking must be imprinted on the spatial symmetry of the new eigenmodes, lowering their symmetry to a strongly anisotropic, twofold character. To directly probe this symmetry reduction, we employed polarization-resolved Raman spectroscopy. Because the Raman tensor reflects the underlying symmetry of the excitations, tracking the angular dependence of the polarization allows us to map this reconstruction. This provides a direct optical readout of the mixed-parity states, through their distinctive twofold orthogonal response, as shown in Figure 2d,e,h,i for moderate Mn concentrations.

Second, and crucial for the detection of these mixed states, the breakdown of mirror symmetry modifies the Raman operator itself. While in the pristine case the operator $\mathcal{R}$ is strictly odd with respect to $\mathbb{M}$, allowing transitions only to the odd one–magnon state $|\Psi_-\rangle$ (since the ground state is even), the presence of impurities relaxes this constraint. The impurity-induced operator, $\mathcal{R}_{imp}$, is no longer constrained to be parity-definite. It acquires contributions, denoted as R^+ and R^+_{res}, that are even with respect

to $\mathbb{M}$, a channel formally forbidden in the pure system. These new terms enable a direct coupling to the even component $|\Psi_+\rangle$ of the mixed eigenstates. The generalized impurity-modified operator takes the following phenomenological form:

$$\mathcal{R}_{imp} \propto \frac{1}{2}\cos(2\theta)(R^- + R^+) + (R^-_{res} + R^+_{res}), \tag{10}$$

where $R^-(R^+)$ and $R^-_{res}(R^+_{res})$ yield non-vanishing amplitudes on the $|\Psi_-\rangle$ ($|\Psi_+\rangle$) state only. The theoretical angular dependence derived from Equation (10) is shown in Figure 5b. This profile was obtained by using matrix elements for the Raman operator that are consistent with the experimental intensity ratios of the two one–magnon peaks for the Mn-doped system, specifically for the representative case of $x = 5\%$ at 2.2 eV (Figure 2e,i). Furthermore, a mixing angle $\alpha = \pi/8$ was chosen for the mixed-parity state, as it provides a good agreement with the experimental data. The model successfully reproduces the observed 90° phase shift between the intensities of the two modes. While the impurity-induced local mirror-symmetry breaking is strictly responsible for mixing the parity modes and activating these two distinct excitations, this structural effect alone would still yield an identical, symmetric angular profile for both modes. The observed deviation from this ideal symmetry, manifesting as the specific 90° phase shift between the two excitations, strictly requires the inclusion of the resonant scattering terms. Ultimately, this specific angular response stems from a delicate interplay between the quantum superposition of the mixed-parity states and the amplitudes of the resonant and non-resonant Raman matrix elements (see Note S6 for details).

4 | Conclusion

We have shown that partial substitution of Ru with Mn in Ca_2RuO_4 reconstructs the magnon spectrum and activates one–magnon excitations that are hidden in the undoped material. This effect arises from local mirror-symmetry breaking of the spin–orbital configuration, induced by structural distortions of the RuO_6 octahedra near the dopant, and demonstrates the critical role of spin–orbit–lattice entanglement in shaping collective magnetic excitations. Our findings highlight that spin–orbital magnons are highly sensitive to local structural and electronic perturbations, providing a pathway to control magnetic dynamics beyond conventional spin-only physics. More broadly, the mechanism uncovered here suggests that hidden magnons in a wide range of spin–orbit correlated materials, especially those with large local magnetic moments, could be selectively accessed through dopants, strain, or other pathways for inducing lattice distortions, such as applied electric fields, thereby opening new opportunities to engineer magnonic spectra for quantum and spintronic devices. Finally, our results demonstrate that the mixed–parity character of the coupled magnons gives rise to a remarkable polarization dependence of the magnetic excitations. This manifests as a changeover from fourfold to twofold rotational symmetry, producing a pronounced nematic-like polarization response. The observed symmetry reduction also reflects the intricate interplay between resonant and nonresonant scattering channels and highlights how spin–orbit–lattice entanglement can be exploited to generate magneto–optical effects based on both the symmetry and polarization characteristics of collective magnetic modes in correlated materials.

Author Contributions

M.C., R.F., F.F., C.K., and D.W. conceived the research project. M.C., F.F., C.K., and D.W. designed the study, with contributions from R.F. and A.V. R.F., A.G., V. G., M.L. and A.V. grew and characterized the $Ca_2(Ru,Mn)O_4$ single crystals. D.W. carried out the Raman measurements and performed the data interpretation, F.F., F.G. and M.C. contributed to the data discussion. M.C., F.F., and F.G. proposed the mechanism of symmetry-breaking-induced magnons. M.C., F.F., and F.G. developed the theoretical model, with contributions from W.B.. W.B. carried out the Raman spectrum simulations, with contributions from M.C., F.F., and F.G., M.C., F.F., F.G., and D.W. wrote the manuscript with contributions from all authors.

Acknowledgements

M.C., F.F., R.F., A.G., M.L. and A.V. acknowledge partial support by the Italian Ministry of Foreign Affairs and International Cooperation, grant KR23GR06. F.F. and F.G. acknowledge support from the Italian Ministry of University and Research under the National Recovery and Resilience Plan (NRRP), Call PRIN 2022, funded by the European Union - NextGenerationEU, Mission 4, Component 2, Grant No. 2022TWZ9NR (STIMO)-CUP B53D23004560006. M.C. and A.V. acknowledge support by Italian MUR PRIN 2022 under the Grant No. 2022LP5K7 (BEAT). M.C. and F.F. acknowledge support from PNRR MUR project PE0000023-NQSTI. W.B. acknowledges support by Narodowe Centrum Nauki (NCN, National Science Centre, Poland) Project No. 2021/43/B/ST3/02166. C.K. was supported by the National Research Foundation of Korea (NRF) (Grant No. and NRF-2022R1A3B1077234). D.W. acknowledges support from the Institute of Applied Physics of Seoul National University, from the ITRC Program through the IITP, and from the Global Research Development Center (GRDC) Cooperative Hub Program through the NRF, funded by the (MSIT) (Grant Nos. RS-2024-00437191 and RS-2023-00258359). Part of this research was supported by the G-LAMP Program of the National Research Foundation of Korea (NRF) grant funded by the Ministry of Education (RS-2026-25609336).

Conflicts of Interest

The authors declare no conflicts of interest.

Data Availability Statement

The data that support the findings of this study are available from the corresponding author upon reasonable request.

References

1. A. Georges, L. de Medici, and J. Mravlje, "Strong Correlations from Hund's Coupling," *Annual Review of Condensed Matter Physics* 4, no. 4, 2013 (2013): 137–178, https://doi.org/10.1146/annurev-conmatphys-020911-125045.

2. G. Khaliullin, "Orbital Order and Fluctuations in Mott Insulators," *Progress of Theoretical Physics Supplement* 160 (2005): 155–202, https://doi.org/10.1143/PTPS.160.155.

3. G. Cao and P. Schlottmann, "The Challenge of Spin-Orbit-Tuned Ground States in Iridates: A Key Issues Review," *Reports on Progress in Physics* 81, no. 4 (feb 2018): 042502, https://doi.org/10.1088/1361-6633/aaa979.

4. T. Takayama, J. Chaloupka, A. Smerald, G. Khaliullin, and H. Takagi, "Spin-Orbit-Entangled Electronic Phases in 4d and 5d Transition-Metal Compounds," *Journal of the Physical Society of Japan* 90, no. 6 (2021): 062001, https://doi.org/10.7566/JPSJ.90.062001.

5. D. Pesin and L. Balents, "Mott Physics and Band Topology in Materials with Strong Spin-Orbit Interaction," *Nature Physics* 6, no. 5 (March 2010): 376–381, https://doi.org/10.1038/nphys1606.

6. C. S. Alexander, G. Cao, V. Dobrosavljevic, et al., "Destruction of the Mott Insulating Ground State of Ca_2RuO_4 by a Structural Transition," *Physical Review B* 60 (Sep 1999): R8422–R8425, https://doi.org/10.1103/PhysRevB.60.R8422.

7. S. Nakatsuji and Y. Maeno, "Quasi-Two-Dimensional Mott Transition System $Ca_{2-x}Sr_xRuO_4$," *Physical Review Letters* 84 (Mar 2000): 2666–2669, https://doi.org/10.1103/PhysRevLett.84.2666.

8. S. Riccó, M. Kim, A. Tamai, et al., "In Situ Strain Tuning of the Metal-Insulator-Transition of Ca_2RuO_4 in Angle-Resolved Photoemission Experiments," *Nature Communications* 9 (2018): 4535, https://doi.org/10.1038/s41467-018-06945-0.

9. O. Friedt, M. Braden, G. André, P. Adelmann, S. Nakatsuji, and Y. Maeno, "Structural and Magnetic Aspects of the Metal-Insulator Transition in $Ca_{2-x}Sr_xRuO_4$," *Physical Review B* 63 (Apr 2001): 174432, https://doi.org/10.1103/PhysRevB.63.174432.

10. G. Cuono and C. Autieri, "Mott Insulator Ca_2RuO_4 Under External Electric Field," *Materials* 15, no. 19 (2022): 6657, https://doi.org/10.3390/ma15196657.

11. N. Gauquelin, F. Forte, D. Jannis, et al., "Pattern Formation by Electric-Field Quench in a Mott Crystal," *Nano Letters* 23, no. 17 (2023): 7782–7789, https://doi.org/10.1021/acs.nanolett.3c00574.

12. G. Cuono, F. Forte, A. Romano, and C. Noce, "Emerging New Phases in Correlated Mott Insulator Ca_2RuO_4," *Journal of Physics: Condensed Matter* 37, no. 5 (nov 2024): 053002, https://doi.org/10.1088/1361-648X/ad906d.

13. D. Sutter, C. Fatuzzo, S. Moser, et al., "Hallmarks of Hund's Coupling in the Mott Insulator Ca_2RuO_4," *Nature Communications* 8 (2017): 15176, https://doi.org/10.1038/ncomms15176.

14. L. Das, F. Forte, R. Fittipaldi, et al., "Spin-Orbital Excitations in Ca_2RuO_4 Revealed by Resonant Inelastic X-Ray Scattering," *Physical Review X* 8, no. 1 (March 2018): 011048, https://doi.org/10.1103/PhysRevX.8.011048.

15. F. Nakamura, H. Ogura, T. Sakami, and T. Suzuki, "Unique Itinerant Ferromagnetism in 4*d* Electron System Ca_2RuO_4," *JPS Conference Proceedings* 38 (2023): 011128, https://doi.org/10.7566/JPSCP.38.011128.

16. A. Jain, M. Krautloher, J. Porras, et al., "Higgs Mode and its Decay in a Two-Dimensional Antiferromagnet," *Nature Physics* 13, no. 7 (July 2017): 633–637, https://doi.org/10.1038/nphys4077.

17. W. Brzezicki, F. Forte, C. Noce, M. Cuoco, and A. M. Oleś, "Spin-Orbital Mechanisms for Negative Thermal Expansion in Ca_2RuO_4," *Physical Review B* 107 (Mar 2023): 104403, https://doi.org/10.1103/PhysRevB.107.104403.

18. F. Nakamura, M. Sakaki, Y. Yamanaka, S. Tamaru, T. Suzuki, and Y. Maeno, "Electric-Field-Induced Metal Maintained by Current of the Mott Insulator Ca_2RuO_4," *Scientific Reports* 3, no. 1 (2013): 2536.

19. I. Terasaki, I. Sano, K. Toda, et al., "Non-Equilibrium Steady State in the Mott Insulator Ca_2RuO_4," *Journal of the Physical Society of Japan* 89, no. 9 (2020): 093707.

20. J. Bertinshaw, N. Gurung, P. Jorba, et al., "Unique Crystal Structure of Ca_2RuO_4 in the Current Stabilized Semimetallic State," *Physical Review Letters* 123 (Sep 2019): 137204, https://doi.org/10.1103/PhysRevLett.123.137204.

21. C. Cirillo, V. Granata, G. Avallone, et al., "Emergence of a Metallic Metastable Phase Induced by Electrical Current in Ca_2RuO_4," *Physical Review B* 100 (Dec 2019): 235142, https://doi.org/10.1103/PhysRevB.100.235142.

22. D. Curcio, C. E. Sanders, A. Chikina, et al., "Current-driven Insulator-to-Metal Transition Without Mott Breakdown in Ca_2RuO_4," *Physical Review B* 108 (Oct 2023): L161105, https://doi.org/10.1103/PhysRevB.108.L161105.

23. C. T. Suen, I. Marković, M. Zonno, et al., "Electronic Response of a Mott Insulator at a Current-Induced Insulator-to-Metal Transition," *Nature Physics* 20 (2024): 1757–1763.

24. J. Zhang, A. S. McLeod, Q. Han, et al., "Nano-Resolved Current-Induced Insulator-Metal Transition in the Mott Insulator Ca_2RuO_4," *Physical Review X* 9 (Feb 2019): 011032, https://doi.org/10.1103/PhysRevX.9.011032.

25. K. Fürsich, J. Bertinshaw, P. Butler, M. Krautloher, M. Minola, and B. Keimer, "Raman Scattering from Current-Stabilized Nonequilibrium Phases in Ca_2RuO_4," *Physical Review B* 100 (Aug 2019): 081101, https://doi.org/10.1103/PhysRevB.100.081101.

26. V. K. Bhartiya, R. Hartmann, F. Forte, et al., "Evidence of Electronic States Driving Current-Induced Insulator-to-Metal Transition," (2025), arxiv:2504.17871.

27. S. Nakatsuji, S. Ikeda, and Y. Maeno, "Ca_2RuO_4: New Mott Insulators of Layered Ruthenate," *Journal of the Physical Society of Japan* 66, no. 7 (1997): 1868–1871, https://doi.org/10.1143/JPSJ.66.1868.

28. G. Cao, S. McCall, M. Shepard, J. E. Crow, and R. P. Guertin, "Magnetic and Transport Properties of Single-Crystal Ca_2RuO_4 : Relationship to Superconducting Sr_2RuO_4," *Physical Review B* 56 (Aug 1997): R2916–R2919, https://doi.org/10.1103/PhysRevB.56.R2916.

29. M. Braden, G. André, S. Nakatsuji, and Y. Maeno, "Crystal and Magnetic Structure of Ca_2RuO_4 : Magnetoelastic Coupling and the Metal-Insulator Transition," *Physical Review B* 58, no. 2 (Jul 1998): 847–861, https://doi.org/10.1103/PhysRevB.58.847.

30. S.-M. Souliou, J. Chaloupka, G. Khaliullin, et al., "Raman Scattering from Higgs Mode Oscillations in the Two-Dimensional Antiferromagnet Ca_2RuO_4," *Physical Review Letters* 119 (Aug 2017): 067201, https://doi.org/10.1103/PhysRevLett.119.067201.

31. D. G. Porter, V. Granata, F. Forte, et al., "Magnetic Anisotropy and Orbital Ordering in Ca_2RuO_4," *Physical Review B* 98 (Sep 2018): 125142, https://doi.org/10.1103/PhysRevB.98.125142.

32. C. G. Fatuzzo, M. Dantz, S. Fatale, et al., "Spin-Orbit-Induced Orbital Excitations in Sr_2RuO_4 and Ca_2RuO_4 : A Resonant Inelastic X-Ray Scattering Study," *Physical Review B* 91 (Apr 2015): 155104, https://doi.org/10.1103/PhysRevB.91.155104.

33. H. Gretarsson, H. Suzuki, H. Kim, et al., "Observation of Spin-Orbit Excitations and Hund's Multiplets in Ca_2RuO_4," *Physical Review B* 100 (Jul 2019): 045123, https://doi.org/10.1103/PhysRevB.100.045123.

34. G. Khaliullin, "Excitonic Magnetism in Van Vleck–type d^4 Mott Insulators," *Physical Review Letters* 111 (Nov 2013): 197201, https://doi.org/10.1103/PhysRevLett.111.197201.

35. F. Forte, M. Cuoco, and C. Noce, "Field-Induced Orbital Patterns in Ferromagnetic Layered Ruthenates," *Physical Review B* 82 (2010): 155104, https://doi.org/10.1103/PhysRevB.82.155104.

36. T. Feldmaier, P. Strobel, M. Schmid, P. Hansmann, and M. Daghofer, "Excitonic Magnetism at the Intersection of Spin-Orbit Coupling and Crystal-Field Splitting," *Physical Review Research* 2 (Aug 2020): 033201, https://doi.org/10.1103/PhysRevResearch.2.033201.

37. P. M. Sarte, C. Stock, B. R. Ortiz, K. H. Hong, and S. D. Wilson, "Van Vleck Excitons in Ca_2RuO_4," *Physical Review B* 102 (Dec 2020): 245119, https://doi.org/10.1103/PhysRevB.102.245119.

38. P. Steffens, O. Friedt, P. Alireza, et al., "High-Pressure Diffraction Studies on Ca_2RuO_4," *Physical Review B* 72 (Sep 2005): 094104, https://doi.org/10.1103/PhysRevB.72.094104.

39. T. F. Qi, O. B. Korneta, S. Parkin, L. E. De Long, P. Schlottmann, and G. Cao, "Negative Volume Thermal Expansion Via Orbital and Magnetic Orders in $Ca_2Ru_{1-x}Cr_xO_4$ $(0 < x < 0.13)$," *Physical Review Letters* 105 (Oct 2010): 177203, https://doi.org/10.1103/PhysRevLett.105.177203.

40. S. Chi, F. Ye, G. Cao, H. Cao, and J. A. Fernandez-Baca, "Competition of Three-Dimensional Magnetic Phases in $Ca_2Ru_{1-x}Fe_xO_4$: A Structural Perspective," *Physical Review B* 102 (Jul 2020): 014452, https://doi.org/10.1103/PhysRevB.102.014452.

41. D. G. Porter, F. Forte, V. Granata, et al., "Guiding Antiferromagnetic Transitions in Ca_2RuO_4," *Scientific Reports* 12, no. 1 (Jun 2022): 10957, https://doi.org/10.1038/s41598-022-14932-1.

42. D. Tian, L. Miao, L. Si, et al., "Tuning the Electronic and Magnetic States of Ca_2RuO_4 with Proton Evolution," *Physical Review Materials* 8 (Jul 2024): 074408, https://doi.org/10.1103/PhysRevMaterials.8.074408.

43. S. Kunkemöller, E. Komleva, S. V. Streltsov, et al., "Magnon Dispersion in $Ca_2Ru_{1-x}Ti_xO_4$: Impact of Spin-Orbit Coupling and Oxygen Moments," *Physical Review B* 95 (Jun 2017): 214408, https://doi.org/10.1103/PhysRevB.95.214408.

44. D. Pincini, S. Boseggia, R. Perry, et al., "Persistence of Antiferromagnetic Order upon La Substitution in the $4d^4$ Mott Insulator Ca_2RuO_4," *Physical Review B* 98 (Jul 2018): 014429, https://doi.org/10.1103/PhysRevB.98.014429.

45. W. Brzezicki, A. M. Oleś, and M. Cuoco, "Spin-Orbital Order Modified by Orbital Dilution in Transition-Metal Oxides: From Spin Defects to Frustrated Spins Polarizing Host Orbitals," *Physical Review X* 5 (Mar 2015): 011037, https://doi.org/10.1103/PhysRevX.5.011037.

46. W. Brzezicki, F. Forte, C. Noce, M. Cuoco, and A. M. Oleś, "Tuning Crystal Field Potential by Orbital Dilution in Strongly Correlated d^4 Oxides," *Journal of Superconductivity and Novel Magnetism* 33, no. 8 (Aug 2020): 2375–2381, https://doi.org/10.1007/s10948-019-05386-0.

47. W.-H. Li, C. H. Perry, J. B. Sokoloff, V. Wagner, M. E. Chen, and G. Shirane, "Polarized Neutron Studies of Forbidden Magnons in the Two-Dimensional Ferromagnet K_2CuF_4," *Physical Review B* 35 (Feb 1987): 1891–1898, https://doi.org/10.1103/PhysRevB.35.1891.

48. A. Etesamirad, J. Kharlan, R. Rodriguez, I. Barsukov, and R. Verba, "Controlling Selection Rules for Magnon Scattering in Nanomagnets by Spatial Symmetry Breaking," *Physical Review Applied* 19 (Apr 2023): 044087, https://doi.org/10.1103/PhysRevApplied.19.044087.

49. T. W. J. Metzger, K. A. Grishunin, C. Reinhoffer, et al., "Magnon-Phonon Fermi Resonance in Antiferromagnetic CoF_2," *Nature Communications* 15, no. 1 (Jun 2024): 5472, https://doi.org/10.1038/s41467-024-49716-w.

50. G. Gitgeatpong, Y. Zhao, P. Piyawongwatthana, et al., "Nonreciprocal Magnons and Symmetry-Breaking in the Noncentrosymmetric Antiferromagnet," *Physical Review Letters* 119 (Jul 2017): 047201, https://doi.org/10.1103/PhysRevLett.119.047201.

51. S. M. Winter, K. Riedl, P. A. Maksimov, A. L. Chernyshev, A. Honecker, and R. Valentí, "Breakdown of Magnons in a Strongly Spin-Orbital Coupled Magnet," *Nature Communications* 8, no. 1 (Oct 2017): 1152, https://doi.org/10.1038/s41467-017-01177-0.

52. H.-H. Kim, K. Ueda, S. Nakata, et al., "Giant Stress Response of Terahertz Magnons in a Spin-Orbit Mott Insulator," *Nature Communications* 13, no. 1 (Nov 2022): 6674, https://doi.org/10.1038/s41467-022-34375-6.

53. X. Chen, Y. Liu, P. Liu, et al., "Unconventional Magnons in Collinear Magnets Dictated by Spin Space Groups," *Nature* 640, no. 8058 (Apr 2025): 349–354, https://doi.org/10.1038/s41586-025-08715-7.

54. Y. Zhang, X. Wu, B. Lyu, et al., "Magnetic Order-Induced Polarization Anomaly of Raman Scattering in 2D Magnet CrI_3," *Nano Letters* 20, no. 1 (December 2019): 729–734.

55. A. McCreary, J. R. Simpson, T. T. Mai, et al., "Quasi-Two-Dimensional Magnon Identification in Antiferromagnetic $FePS_3$ via Magneto-Raman Spectroscopy," *Physical Review B* 101 (Feb 2020): 064416, https://doi.org/10.1103/PhysRevB.101.064416.

56. A. Glamazda, P. Lemmens, S.-H. Do, Y. S. Choi, and K.-Y. Choi, "Raman Spectroscopic Signature of Fractionalized Excitations in the Harmonic-Honeycomb Iridates β- and γ-Li_2IrO_3," *Nature Communications* 7, no. 1 (Jul 2016): 12286, https://doi.org/10.1038/ncomms12286.

57. Y. Yang, M. Li, I. Rousochatzakis, and N. B. Perkins, "Non-Loudon-Fleury Raman scattering in Spin-Orbit Coupled Mott Insulators," *Physical Review B* 104 (Oct 2021): 144412, https://doi.org/10.1103/PhysRevB.104.144412.

58. J. H. Lee, D. Wulferding, J. Kim, D. Song, S. R. Park, and C. Kim, "Linear Scaling Relationship of Néel Temperature and Dominant Magnons in Pyrochlore Ruthenates," *Physical Review B* 108 (Aug 2023): 054443, https://doi.org/10.1103/PhysRevB.108.054443.

59. D. Wulferding, J. Kim, M. K. Kim, et al., "Collective Magnetic Higgs Excitation in a Pyrochlore Ruthenate," *npj Quantum Materials* 8, no. 1 (Aug 2023): 40, https://doi.org/10.1038/s41535-023-00572-9.

60. H. Rho, S. L. Cooper, S. Nakatsuji, H. Fukazawa, and Y. Maeno, "Lattice Dynamics and the Electron-Phonon Interaction in Ca_2RuO_4," *Physical Review B* 71 (Jun 2005): 245121, https://doi.org/10.1103/PhysRevB.71.245121.

61. S.-M. Souliou, J. Chaloupka, G. Khaliullin, et al., "Raman Scattering from Higgs Mode Oscillations in the Two-Dimensional Antiferromagnet Ca_2RuO_4," *Physical Review Letters* 119, no. 6 (August 2017): 067201, https://doi.org/10.1103/PhysRevLett.119.067201.

62. K. Ueda, R. Kaneko, A. Subedi, et al., "Phonon Anomalies in Pyrochlore Iridates Studied by Raman Spectroscopy," *Physical Review B* 100 (Sep 2019): 115157, https://doi.org/10.1103/PhysRevB.100.115157.

63. Y. Tian, M. J. Gray, H. Ji, R. J. Cava, and K. S. Burch, "Magneto-Elastic Coupling in a Potential Ferromagnetic 2D Atomic Crystal," *2D Materials* 3, no. 2 (jun 2016): 025035, https://doi.org/10.1088/2053-1583/3/2/025035.

64. P. A. Fleury and R. Loudon, "Scattering of Light by One- and Two-Magnon Excitations," *Physical Review* 166 (Feb 1968): 514–530, https://doi.org/10.1103/PhysRev.166.514.

65. B. S. Shastry and B. I. Shraiman, "Theory of Raman Scattering in Mott-Hubbard Systems," *Physical Review Letters* 65 (Aug 1990): 1068–1071, https://doi.org/10.1103/PhysRevLett.65.1068.

66. T. P. Devereaux and R. Hackl, "Inelastic Light Scattering from Correlated Electrons," *Reviews of Modern Physics* 79 (Jan 2007): 175–233, https://doi.org/10.1103/RevModPhys.79.175.

67. A. V. Chubukov and D. M. Frenkel, "Resonant Two-Magnon Raman Scattering in Antiferromagnetic Insulators," *Physical Review Letters* 74 (Apr 1995): 3057–3060, https://doi.org/10.1103/PhysRevLett.74.3057.

68. H. Liu and G. Khaliullin, "Pseudo-Jahn-Teller Effect and Magnetoelastic Coupling in Spin-Orbit Mott Insulators," *Physical Review Letters* 122 (Feb 2019): 057203, https://doi.org/10.1103/PhysRevLett.122.057203.

Supporting Information

Additional supporting information can be found online in the Supporting Information section.

Supporting File 1: advs78597-sup-0001-SuppMat.pdf.

Supporting File 2: advs78597-sup-0002-SuppMat.bib.